Accuracy of Terrain Following Coordinates over Isolated Mountain: Steep Mountain Model Intercomparison Project (St-MIP)

Takehiko SATOMURA[*], Toshiki IWASAKI[**], Kazuo SAITO[***]
Chiashi MUROI[****] and Kazuhisa TSUBOKI[*****]

[*] Graduate School of Science, Kyoto University

[**] Graduate School of Science, Tohoku University

[***] Meteorological Research Institute
Present affiliation: Numerical Prediction Division, Japan Meteorological Agency

[****] Numerical Prediction Division, Japan Meteorological Agency
Present affiliation: Meteorological Research Institute

[*****] Hydrospheric Atmospheric Research Center, Nagoya University

Synopsis

Following the recent rapid increase of computational power, resolutions of atmospheric numerical models increase and steep slopes are resolved in models in mountainous areas. To examine the accuracy of the z^* coordinates, which is one of the most common coordinates over complex terrain for atmospheric models and to study the ability of representation of flows over steep slope, a Steep Mountain Model Intercomparison Project (St-MIP) was completed with three nonhydrostatic atmospheric models. Mountain waves over bell-shaped mountains with various half-widths and heights ranging from 0.6 to more than 45 degrees of averaged inclination angles were compared with theoretical calculations and also among models. It is shown that models using the z^* coordinates simulates waves unexpectedly well over very steep mountains provided that the horizontal grid size is small enough to represent the mountain shape smoothly. However, only a model which uses implicit method both in the horizontal and vertical direction cannot complete the time integration.

Keywords: steep slope, accuracy, terrain following coordinates, mountain wave, St-MIP

1. Introduction

Recently, resolutions of atmospheric numerical models increase significantly with the increase of computer power. The increase of horizontal resolution permits the model's representation of steep slopes over complex terrain.

In atmospheric models, the terrain following coordinates called z^* coordinates

$$z^* = z_T \frac{z - z_s}{z_T - z_s} \qquad (1)$$

where z_T is the top of the model domain and z_s is the surface terrain height, is commonly employed. It was shown that the z^* coordinates produced spurious vertical velocity just over the steep mountain (Satomura, 1989). Although the grid resolution of the model used by Satomura (1989) was 500 m, it was not small enough to resolve the steep mountain precisely. Therefore, It is still unclear whether the spurious vertical velocity found by Satomura (1989) was caused by the truncation error of z^* coordinates over the steep slope itself or by a multiplier effect with the bad representation of the mountain.

The model intercomparison project named "St-MIP" was planned to clarify the model ability in representing flow over steep mountain by comparing simulated results of different models. All models participated in St-MIP used the z^* coordinates.

In this paper, we present main results of the model intercomparison.

2. Participated models

Three nonhydrostatic compressible models participated in St-MIP: MRI/NPD-NHM, CReSS and TSO. The MRI/NPD-NHM was developed at Meteorological Research Institute and Numerical Prediction Division of Japan Meteorology Agency (Saito et al., 2001). It uses fully compressible hydrodynamic equations and has options of a horizontally explicit and vertically implicit method (hereafter, HE-VI) and also a horizontally and vertically implicit method (HI-VI) of time integration. The CReSS model was developed by a cooperation of Hydrospheric Atmospheric Research Center, Nagoya University, and Research Organization for Information Science \& Technology (Tsuboki and Sakakibara, 2001). The CReSS bases on the ARPS developed at the CAPS (Xue et al., 1995) and uses quasi-compressible equations. The TSO model was developed at Meteorological Research Institute (Satomura, 1989). It uses fully compressible equations and the horizontally explicit and vertically implicit method of time integration. All three models uses the leap-frog time integration scheme with variations of time splitting method.

3. Simulation conditions

Table 1 shows the simulation conditions of St-MIP. There are 7 cases (A1 to A4 and D1 to D3) to be simulated. All cases include one bell-shaped mountain

$$z_s = \frac{h}{1 + (x - x_0)^2 / a^2} \qquad (2)$$

at the center of the domain, x_0, where h is the height of the mountain and a is the half width of the mountain. Here, the Brant-Väisäla frequency, N, was not specified, but constant horizontal velocity, U=10 m s^{-1}, and Scorer parameter $l=U/N$ were specified for each case.

The horizontal grid increment, dx, was determined to be smaller than 1/5 of the half width of the mountain, a, to resolve the mountain accurately. One exception of this rule was case D3 where dx was a/4 owing to save computational time. The vertical grid increment, dz, was determined to be smaller than dx and also to capture the vertical structure of flow over the mountain. The horizontal grid number is more than 2000 to prevent cyclic lateral boundaries modifying the simulated results. The height of integration domain is higher than 15 km except cases A3 and A4 where no noticeable vertically propagating wave won't appear. If one's model requires a kind of sponge layer to diffuse reflected gravity waves from the upper free-slip rigid wall boundary, it should be placed at higher than 10 km. The lower boundary was specified to be free-slip and rigid surface.

The last column is the non dimensional mountain height scaled by the Scorer parameter, hl, which indicates the applicability of linear theory. When $hl \ll 1$ (series A), the mountain is so small compared with the vertical stratification that the linear theory has a good accuracy. When $hl \approx 1$ (series D), the mountain is high enough to take into account the nonlinear effects (e.g. Smith, 1977).

The second column from the last shows the parameter al indicating what type of disturbances would be observed in each case (e.g. Smith, 1977). When $al \gg 1$ (case A1), linear theory predicts that nearly hydrostatically balanced mountain waves will appear, while nonhydrostatic mountain waves should be observed when $al \approx 1$ (case A2). When $al \ll 1$, the linear theory predicts that wave structures diminish and simple flow which climbs over and goes down the mountain will be simulated.

The column θ is the average slope angle of the mountain calculated from the height and the half width of the mountain. Case A1 is very gentle slope and cases A4 and D2 are 45°.

The final integration time was specified to the each case: 300 min, 100 min, 20 min and 10 min for A1, A2, A3 and A4, respectively, and 100 min for series D. These values were determined to assure

Table 1. Simulation conditions

	a (m)	h (m)	l (m^{-1})	dx, dz (m)	θ (deg)	$a*l$	$h*l$
A1	5000	100	2x10^{-3}	1000, 250	0.57	10	0.2
A2	500	100	2x10^{-3}	100, 100	5.7	1	0.2
A3	100	100	2x10^{-3}	20, 20	26.5	0.2	0.2
A4	50	100	2x10^{-3}	5, 5	45	0.1	0.2
D1	500	500	1x10^{-3}	50, 50	26.5	0.5	0.5
D2	250	500	1x10^{-3}	50, 50	45	0.25	0.5

gravity waves forced by the mountain of propagating faraway from the mountain at the end of simulations.

4. Results

4.1 Structures

Figure 1 shows the vertical velocity around the mountain in case A1. For MRI/NPD-NHM, results with the option HI-VI are shown when the results with HE-VI option are the same as those of HI-VI. Results of MRI/NPD-NHM and TSO are the almost identical to the results of the linear theory. The amplitude of waves in CReSS, however, seems to be weaker than other models and linear theory.

Figures 2 and 3 show the vertical velocity in cases A2 and A3, respectively. Model results seem to be identical to the results of the linear theory. In these cases, results of CReSS are similar to those of the other models.

Figure 4 shows the vertical velocity in case A4. In this case, MRI/NPD-NHM with the option HI-VI cannot perform the integration to the end of specified time owing to the unknown reason. The same model with the option HE-VI can, however, complete the time integration. This figure, therefore, shows the results of MRI/NPD-NHM with HE-VI option. Because the mountain is narrow comparing to its height and also the scale of excited disturbances are comparable to the mountain, it was difficult to compare directly patterns of simulated vertical velocity with those of linear theory. It is possible to say, however, that the patterns of vertical velocity of models are similar to the linear theory.

Figures 5 and 6 show the vertical velocity in cases D1 and D2, respectively. Even in these highly nonlinear cases, patterns of vertical velocity simulated by the models are similar to the linear theory, although theoretically calculated amplitude of vertical velocity in case D2 is noticeably smaller than that of simulated results. This discrepancy is perhaps caused by the nonlinear effects of the mountain. The model MRI/NPD-NHM with the option HI-VI again failed to complete the time integration in case D2, while that with HE-VI could complete.

4.2 Momentum flux

One of the quantitative tests of representation of gravity waves is comparison of simulated momentum flux

$$M \equiv \int \rho u'w'dx , \qquad (3)$$

where dashed variables are deviation from the horizontal average, with the true values. To examine the performance of the models strictly, theoretical momentum flux including nonlinear effects (for exam-
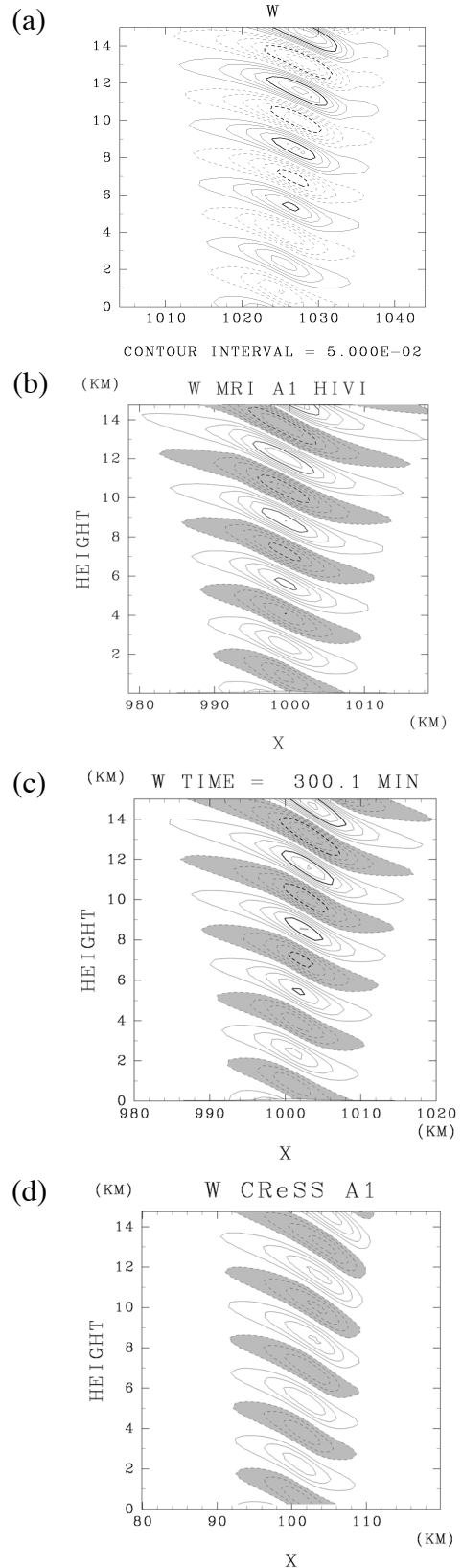

Fig. 1. Vertical velocity in case A1 after 5 hours integration. (a) Linear theory, (b) MRI/NPD-NHM, (c) TSO, and (d) CReSS. Solid lines are positive values, and dashed lines in (a) and shaded areas in (b)-(d) are negative values. Contour interval is 0.05 m s^{-1}
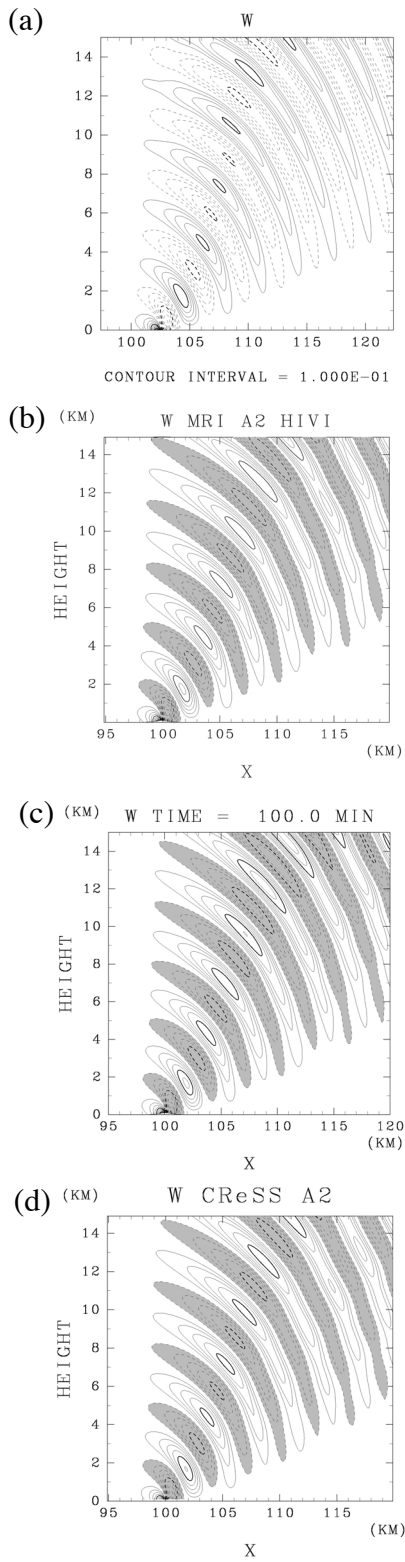
(a)

W

CONTOUR INTERVAL = 1.000E-01

(a)

W

CONTOUR INTERVAL = 2.500E-01

(b) (KM)

W MRI A2 HIVI

HEIGHT

X (KM)

(b) (KM)

W MRI A3 HIVI

HEIGHT

X (KM)

(c) (KM)

W TIME = 100.0 MIN

HEIGHT

X (KM)

(c) (KM)

W TIME = 20.0 MIN

HEIGHT

X (KM)

(d) (KM)
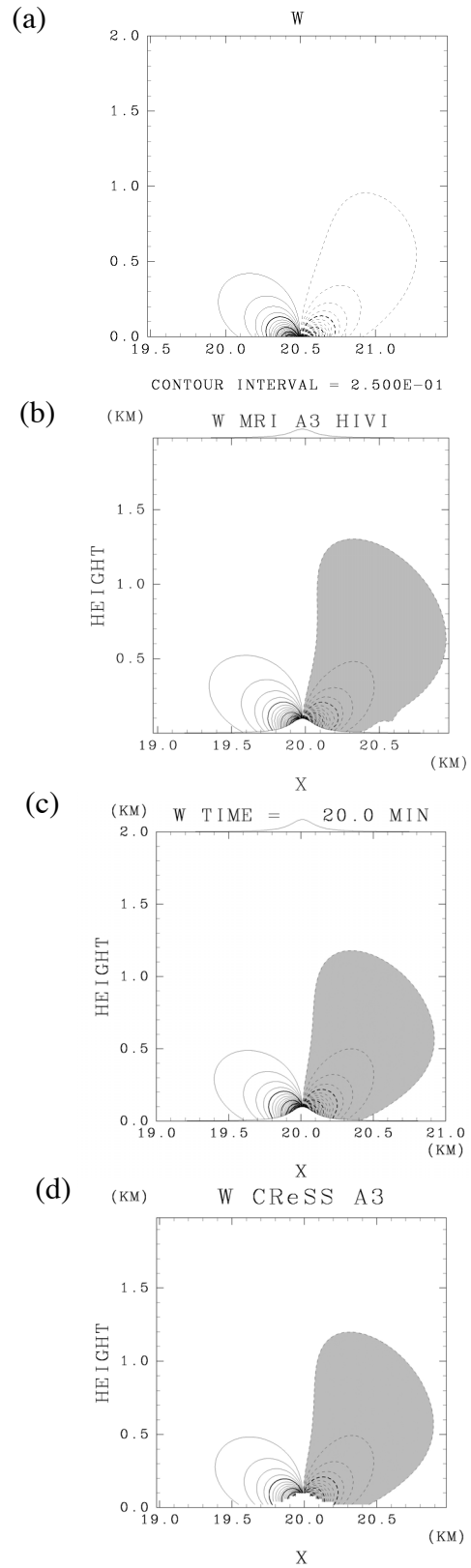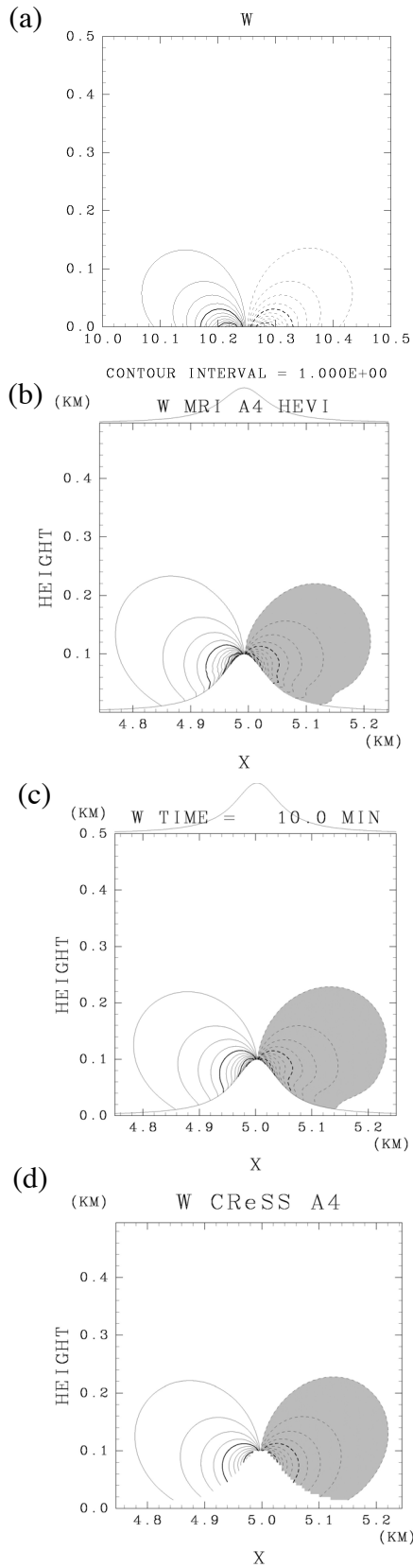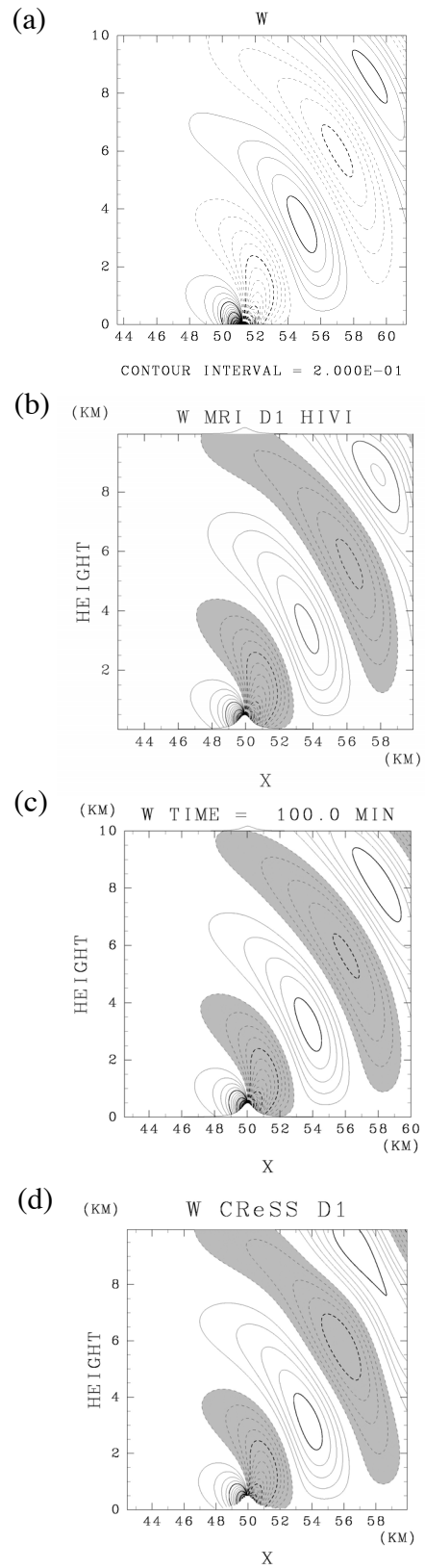
W CReSS A2

HEIGHT

X (KM)

(d) (KM)

W CReSS A3

HEIGHT

X (KM)

Fig. 2. Same as Fig. 1 except case A2
and after 100 min integration.
Contour interval is 0.1 m s^{-1}

Fig. 3. Same as Fig. 1 except case A3
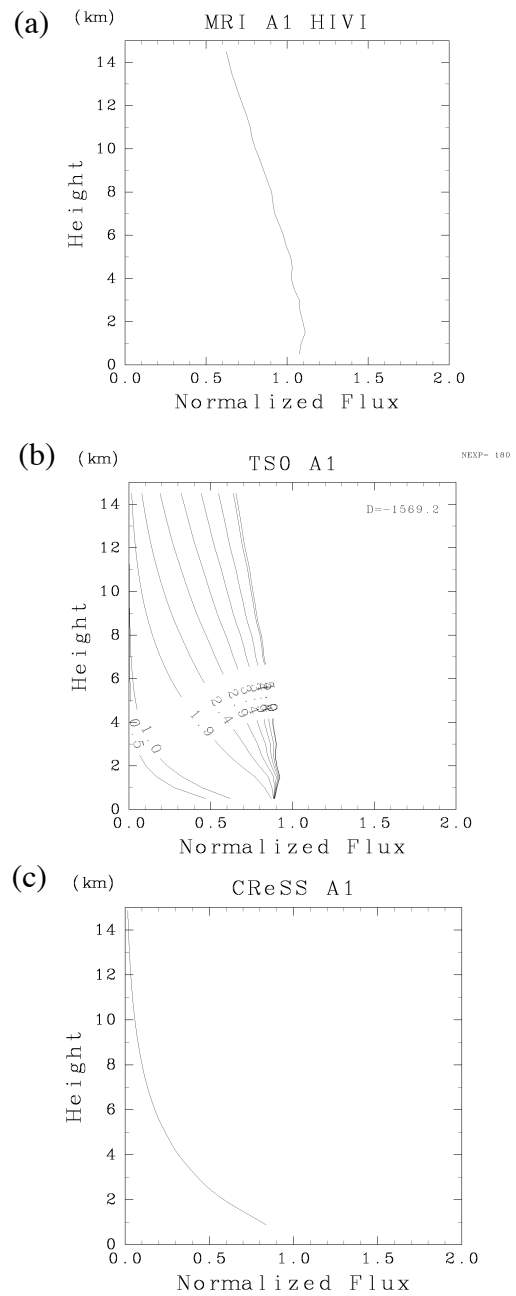and 20 min integration. Contour
interval is 0.25 m s^{-1}

W

CONTOUR INTERVAL = 1.000E+00

(b) (KM)

W MRI A4 HEVI

HEIGHT

X (KM)

(c) (KM)

W TIME = 10.0 MIN

HEIGHT

X (KM)

(d) (KM)

W CReSS A4

HEIGHT

X (KM)

Fig. 4. Same as Fig. 1 except case A4 and after 10 min integration. Contour interval is 1 m s^{-1}

(a)

W

CONTOUR INTERVAL = 2.000E-01

(b) (KM)

W MRI D1 HIVI

HEIGHT

X (KM)

(c) (KM)

W TIME = 100.0 MIN

HEIGHT

X (KM)

(d) (KM)

W CReSS D1

HEIGHT

X (KM)

Fig. 5. Same as Fig. 1 except case D1 and after 100 min integration. Contour interval is 0.2 m s^{-1}

(a)

W

CONTOUR INTERVAL = 5.000E−01

(b) (KM)

W MRI D2 HEVI

HEIGHT

X (KM)

(c) (KM)

W TIME = 100.0 MIN

HEIGHT

X (KM)

(d) (KM)

W CReSS D2

HEIGHT

X (KM)
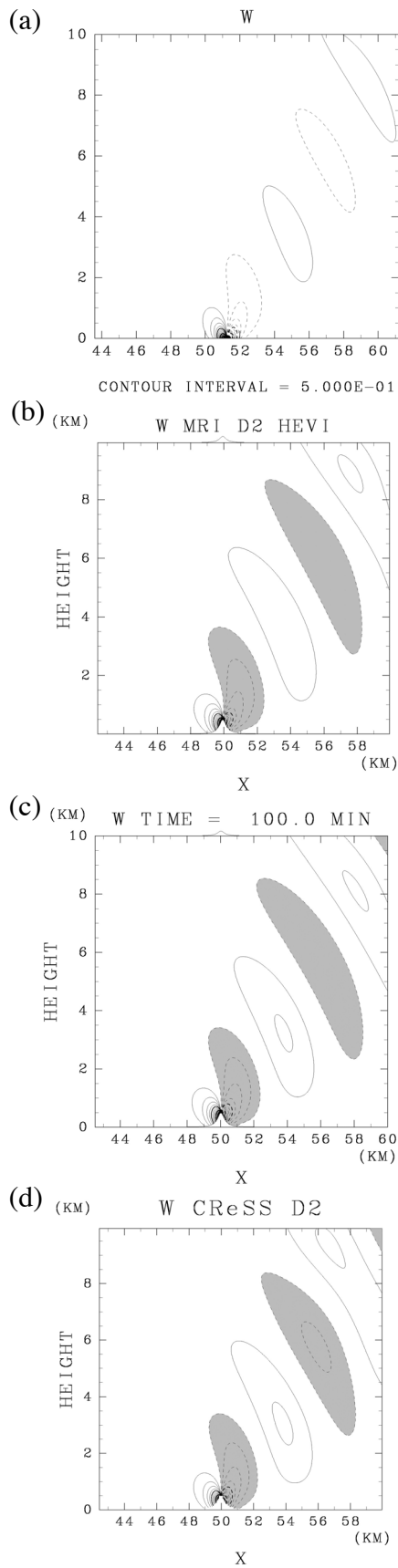
Fig. 6. Same as Fig. 1 except case D2 and after 100 min integration. Contour interval is 0.5 m s^{-1}

(a) (km)

MRI A1 HIVI

Height

Normalized Flux

(b) (km)

TSO A1

NEXP= 180

D=−1569.2

Height

0.5 1.0 1.9 2.4

Normalized Flux

(c) (km)

CReSS A1

Height

Normalized Flux

Fig. 7. Vertical profile of momentum flux by (a) MRI/NPD-NHM, (b) TSO, and (c) CReSS normalized by the flux obtained from the linear theory. Plotted numbers in (b) indicate integration time.

ple, calculated from Long's equation (Long, 1953)) should be used. In this paper, as the first step toward the strict evaluation, we compare the simulated momentum flux with that of linear theory.

Figure 7 shows momentum flux in case A1. Both MRI/NPD-NHM and TSO reproduced the momentum flux similar to the linear theory: normalized value nearly equals to 1 (i.e., equals to the linear theoretical value), and the flux is almost constant with height. However, the momentum flux of CReSS decreases with height rapidly. The vertical group velocity of mountain waves (gravity waves) was smaller in CReSS than the other models and also the linear theory. Therefore, mountain waves did not reach to the high altitude and the momentum flux associated with the mountain waves was much smaller than the other models and the linear theory. The reason why the vertical group velocity was small was not clear yet.

Figure 8 shows the vertical profile of the momentum flux in case A2. Again, models except CReSS reproduced the characteristics of momentum flux profile of mountain waves.

Figures 9 and 10 shows the momentum flux in cases A3 and A4, respectively. In these cases, simulated momentum flux was clearly larger than the linear momentum flux just above the mountain. Because the nonlinear analytical solutions are not yet obtained, we cannot deduce a conclusion that models using $z*$ coordinates produced incorrect momentum flux from these figures.

Figures 11 and 12 show the momentum flux in cases D1 and D2, respectively. In contrast to the small mountain cases A3 and A4, momentum fluxes in these nonlinear cases kept characteristics of those in linear theory. The value was, however, rather larger than that predicted by the linear theory.

5. Conclusion

In order to understand the behavior of truncation error in the $z*$ terrain following coordinates, results of mountain wave simulation under controlled conditions by 3 different models were compared in the frame work of St-MIP. Contrary to the previous presumption, it was not able to notice a clear error in the vertical velocity patterns even in the steepest case where the slope angle was 45°. Both the vertical velocity pattern and the momentum flux over steep and high mountain was smooth and reasonable values.

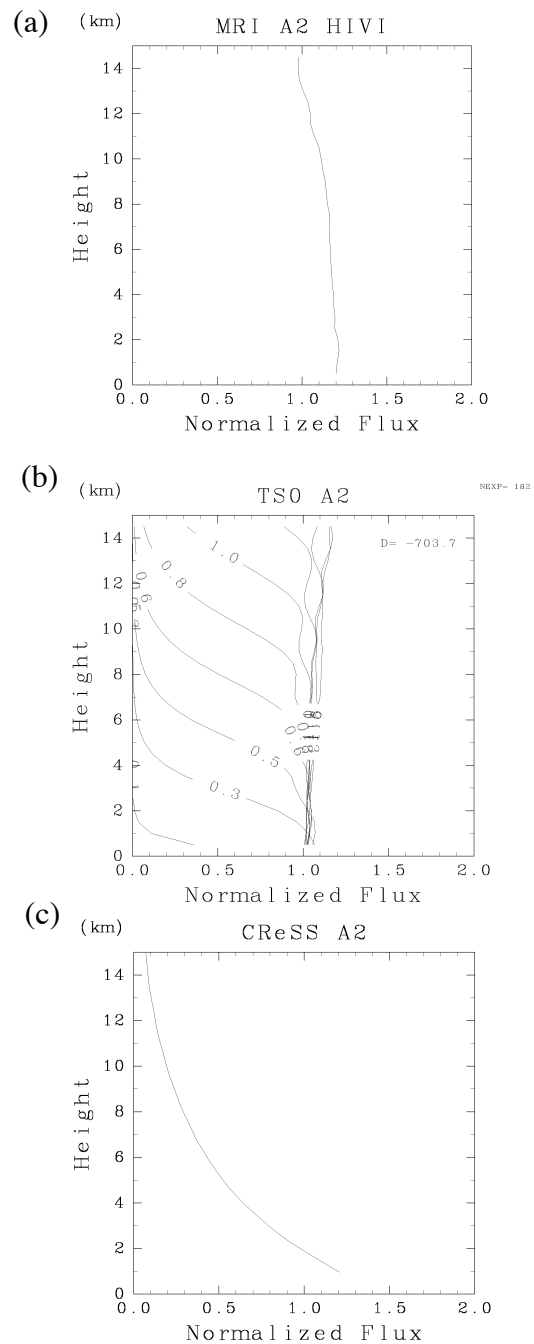We would conclude, therefore, that we can employ the $z*$ coordinates in high resolution models which may contain steep slopes about 45°.

Fig. 8. Same as Fig. 7 except for case A2.

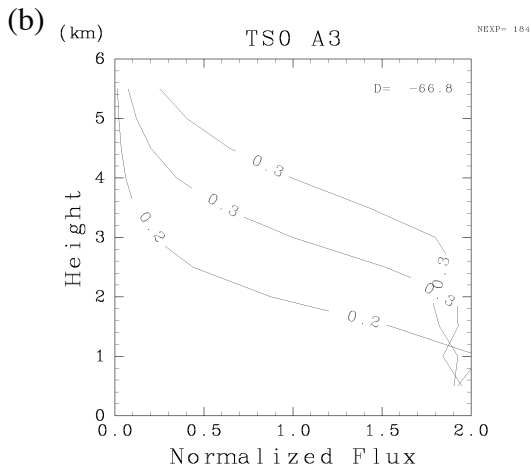(a) (km) MRI A3 HIVI

(b) (km) TSO A3   NEXP= 184

(c) (km) CReSS A3
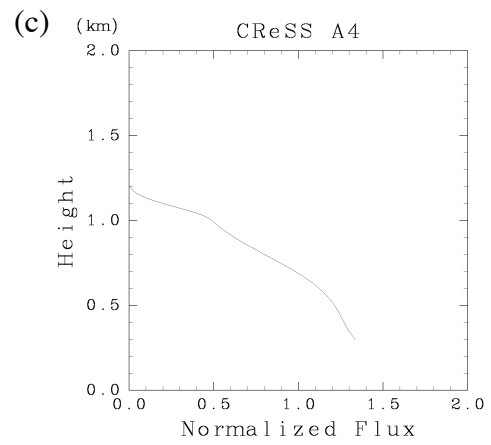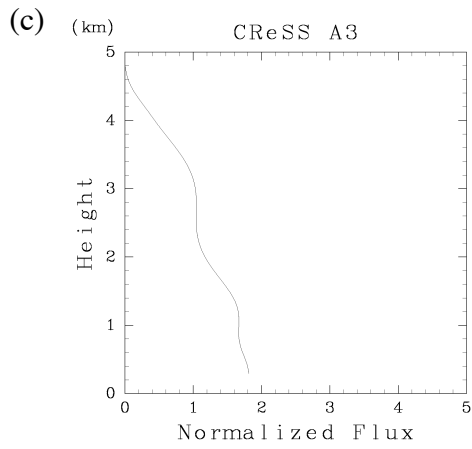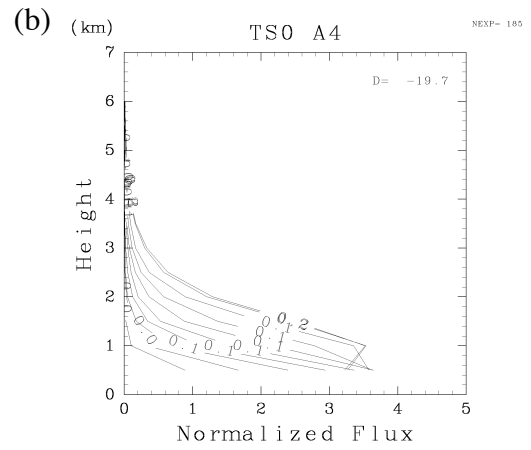
Fig. 9. Same as Fig. 7 except for case A3.

(a) (km) MRI A4 HEVI

(b) (km) TSO A4   NEXP= 185

(c) (km) CReSS A4
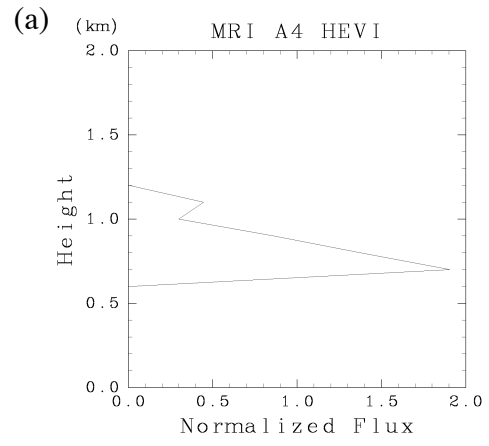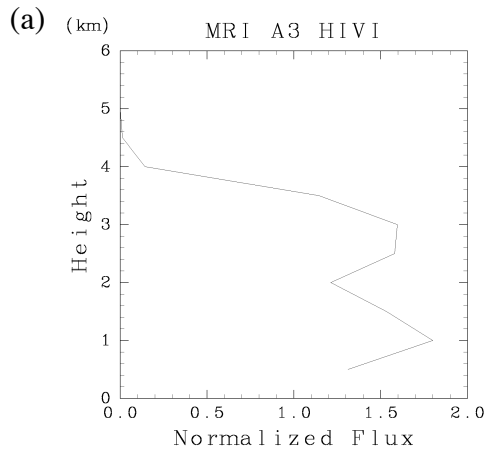
Fig. 10. Same as Fig. 7 except for case A4. The ordinate of (b) covers wider range to indicate the profile of the momentum flux.
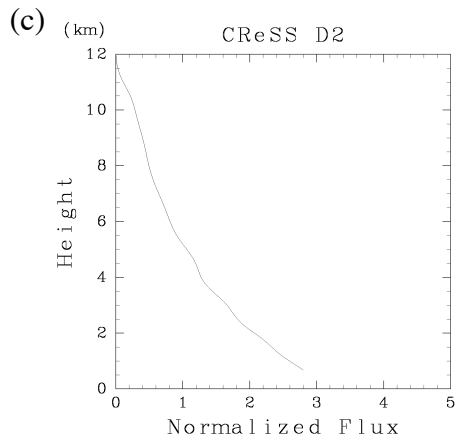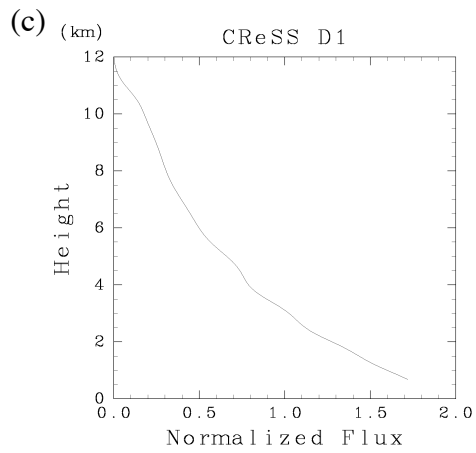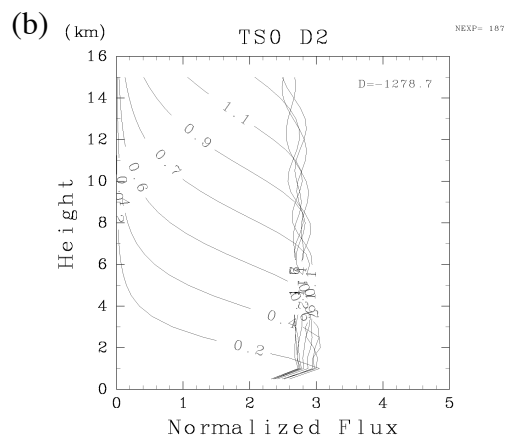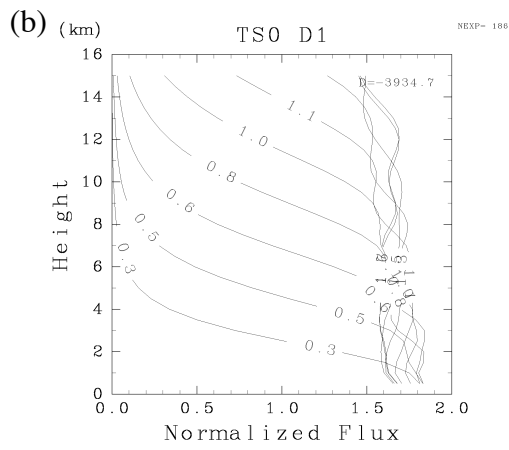
(a) (km)   MRI D1 HIVI

(a) (km)   MRI D2 HEVI

(b) (km)   TS0 D1   NEXP= 186

D=-3934.7

(b) (km)   TS0 D2   NEXP= 187

D=-1278.7

(c) (km)   CReSS D1

(c) (km)   CReSS D2
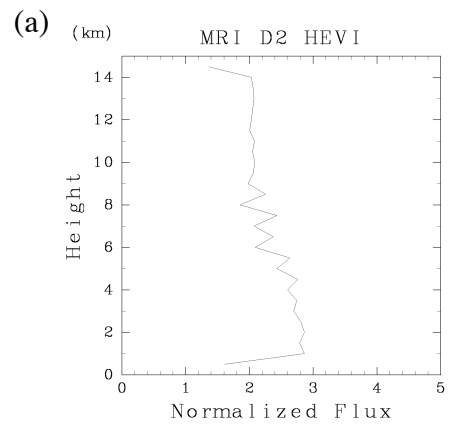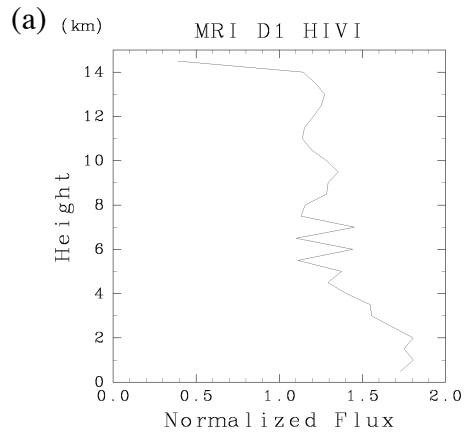
Fig. 11. Same as Fig. 7 except for case D1.

Fig. 12. Same as Fig. 7 except for case D2.

References

Long, R. R., 1953: Some aspects of the flow of stratified fluids. I, A theoretical investigation. *Tellus*, **5**, 42-58.

Saito, K., T. Kato, H. Eito and C. Muroi, 2001: Documentation of the Meteorological Research Institute∨Numerical Prediction Division unified nonhydrostatic model, *Tech. Rep. Meteor. Res. Inst.*, **42**, 133 pp.

Satomura, T., 1989: Compressible flow simulations on numerically generated grids, *J. Meteor. Soc. Japan*, **67**, 473--482.

Smith, R. B., 1977: The influence of mountains on the atmosphere, *Adv. Geophys.*, **21**, 87-230.

Tsuboki, K., and A. Sakakibara, 2001: CReSS Users's Guide, *HyARC, Nagoya University*, 210 pp.

Xue, M., K. K. Droegemeier, V. Wong, A. Shapiro and K. Brewster, 1995: Advanced Regional prediction System ARPS version 4.0 User's Guide, *Center for Analysis and Prediction Storms*, 380 pp.

急斜面モデル比較プロジェクト（St-MIP）による地形準拠座標系の精度検証

里村雄彦 * ・岩崎俊樹 ** ・斉藤和雄 *** ・室井ちあし **** ・坪木和久 *****

* 京都大学大学院理学研究科
** 東北大学大学院理学研究科
*** 気象研究所，現所属：気象庁予報部数値予報課
**** 気象庁予報部数値予報課，現所属：気象研究所
***** 名古屋大学地球水循環研究センター

要　旨

　　最近の急速な計算機パワーの増加にともなって大気数値モデルの分解能が上がり，山岳地域においては高分解能化により急な斜面がモデル内で表現されるようになった。気象学のモデルで一般的な地形準拠座標系である z* 座標系の急斜面上での誤差を調べ，高分解能モデルの再現性を検証するため，圧縮性方程式を用いた 3 種の非静力学大気モデルを比較する研究「急斜面モデル比較プロジェクト（St-MIP）」を行った。その結果，z* 座標系は，孤立山岳を十分解像するほど細かな水平格子間隔を用いる限り，先行研究でして懸念されているほど打ち切り誤差は大きくなく，45 度を超えるような急斜面を持つ孤立山岳上の流れも精度良く表現していることが分かった。また，水平方向と鉛直方向をともに陰解法で解くモデルでは，急斜面での計算ができないことも分かった。

キーワード：非急斜面，精度，地形準拠座標系，山岳波，St-MIP